# Estimating the wheel lateral position of a mechatronic railway running gear with nonlinear wheel–rail geometry

Keck, A.; Schwarz, C.; Meurer, T.; Heckmann, A. & Grether, G.

The "Next Generation Train" (NGT) is a double-deck high speed train concept in light-weight design that has been established as a technical and project framework in which the German Aerospace Center gathers its long-term railway vehicle research. To reduce wheel and rail wear and to enhance the passenger capacity, a mechatronic running gear with independently rotating wheels (IRW) is a key vehicle component under research. This running gear requires an advanced control of the lateral dynamics in order to fully exploit its potential in minimizing wear and noise, but this relies on information on its lateral position relative to the track. In daily railway operation it is difficult to directly measure this displacement of the wheel-pair. However, according to previous work it is possible to design an appropriate observer to estimate the lateral position, but its estimation accuracy highly depends on the chosen sensor configuration. Nevertheless, it was shown that the lateral dynamics of the running were not completely reproduced by the system description especially at suddenly changing directions in the movement of the IRW. In this work the system description is complemented by a nonlinear description of the wheel–rail geometry. Therefore, an observability analysis and an observer synthesis to estimate the lateral position for the nonlinear system of the 1:5 scaled hardware running gear is carried out. For validation purposes an extended Kalman filter with the U-D formalism is implemented at the real-time environment of the testbed and the estimation accuracy of the observer configurations is compared.

Keck, A., Schwarz, C., Meurer, T., Heckmann, A., & Grether, G. (2021). Estimating the wheel lateral position of a mechatronic railway running gear with nonlinear wheel–rail geometry. Mechatronics, 73, S. 102457, ISSN 0957-4158, https://doi.org/10.1016/j.mechatronics.2020.102457

# Estimating the wheel lateral position of a mechatronic railway running gear with nonlinear wheel-rail geometry

Alexander Keck[a,*], Christoph Schwarz[a], Thomas Meurer[b], Andreas Heckmann[a], Gustav Grether[a]

[a] *Institute of System Dynamics and Control, German Aerospace Center, Münchener Str. 20, 82234 Oberpfaffenhofen-Wessling, Germany (e-mail: alexander.keck, christoph.schwarz, gustav.grether, andreas.heckmann@dlr.de)*

[b] *Chair of Automatic Control, Faculty of Engineering, Kiel University, Kaiserstraße 2, 24143 Kiel, Germany (e-mail: tm@tf.uni-kiel.de).*

---

## Abstract

The "Next Generation Train" (NGT) is a double-deck high speed train concept in light-weight design that has been established as a technical and project framework in which the German Aerospace Center gathers its long-term railway vehicle research. To reduce wheel and rail wear and to enhance the passenger capacity, a mechatronic running gear with independently rotating wheels (IRW) is a key vehicle component under research. This running gear requires an advanced control of the lateral dynamics in order to fully exploit its potential in minimizing wear and noise, but this relies on information on its lateral position relative to the track. In daily railway operation it is difficult to directly measure this displacement of the wheel-pair. However, according to previous work it is possible to design an appropriate observer to estimate the lateral position, but its estimation accuracy highly depends on the chosen sensor configuration. Nevertheless, it was shown that the lateral dynamics of the running were not completely reproduced by the system description especially at suddenly changing directions in the movement of the IRW. In this work the system description is complemented by a nonlinear description of the wheel-rail geometry. Therefore, an observability analysis and an observer synthesis to estimate the lateral position for the nonlinear system of the 1:5 scaled hardware running gear is carried out. For validation purposes an extended Kalman filter with the U-D formalism is implemented at the real-time environment of the testbed and the estimation accuracy of the observer configurations is compared.

*Keywords:* Observability analysis, observer design, extended Kalman filter, nonlinear systems, railway, running gear, train

---

## 1. Introduction

This article is motivated and partly based on our previous work [1] which is for the sake of completeness recalled in the following.

### *1.1. NGT project demands*

The "Next Generation Train" (NGT) is an internal project of the German Aerospace Center (DLR). The NGT is equipped with independently rotating wheels (IRW) which makes axle shafts obsolete. The aim of the project is to elaborate a concept for a future high-speed train with a maximum speed of 400 km/h [2]. The NGT project demands 50 % more seats per length and a wheel wear reduction of 20 % as the high-level goals.

Additional space between the wheels is gained, because of the missing axle shaft. This allows also a continuous floor even at the lower deck of a double-deck train design. The positive aspect of the IRWs, is their great potential to reduce wear in curves and also on straight tracks, see [3]. Due to nonexistent kinematic coupling of the velocities of the wheels, the lateral dynamics are unstable [4, 5]. Therefore, to fully utilize the wear reduction potential and to stabilize the lateral dynamics, an active control of the IRWs is required.

To test and to improve the model-based control design, the DLR built a 1:5 scaled version of the running gear on a roller rig, see [2] and [3]. The hardware of the running gear, see Figure 1a, was designed in regard to the similarity laws as stated in [6].

### *1.2. System and sensor setup*

The running gear runs on the 1:5 scaled roller rig of DLR, as shown in the principal sketch in Figure 1b. Four IRWs which are independently driven by in-wheel motors build the running gear. The in-wheel motors are permanently-excited synchronous machines with each being controlled by its own power converters. Each wheel-pair is connected by an axle bridge, which are coupled to the running gear frame via a leaf spring guidance as depicted in Figure 2. The leaf spring is representing the primary suspension of the running gear and thereby enables a yaw motion of the axle bridges. The yaw motion is limited by bump stops. As shown in Figure 1b two revolving rollers with applied rail-profiles of the roller rig are representing the longitudinal motion of the vehicle via its

---

[*] Corresponding author

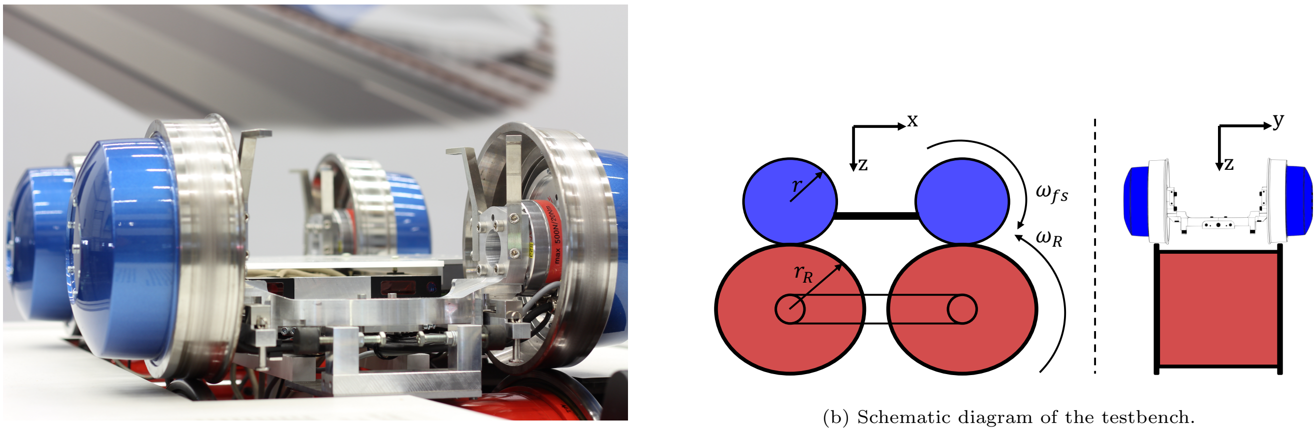

(a) Running gear.

(b) Schematic diagram of the testbench.

Figure 1: Running gear on roller rig.

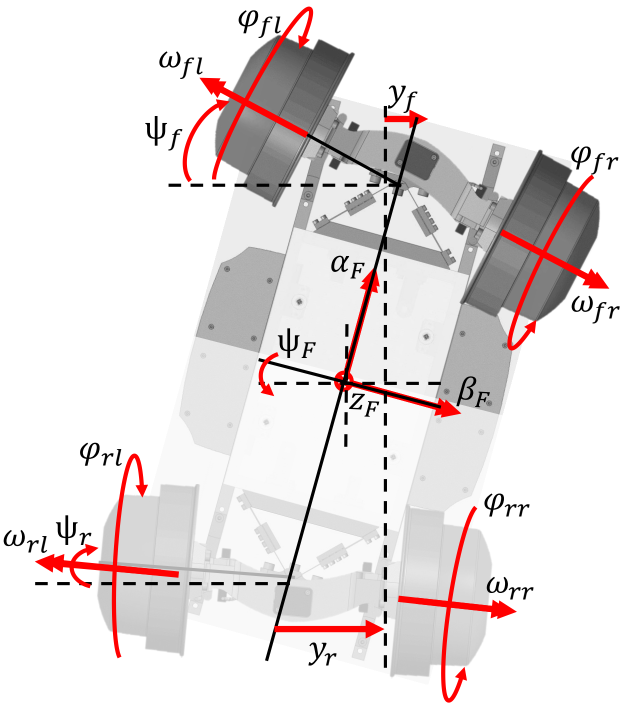

Figure 2: Running gear with all degrees of freedom.

angular velocity $\omega_R$ and the roller radius $r_R$. To prevent the running gear to fall off the rollers, the longitudinal motion is locked by a lemniscate guidance which mounts the central frame to the roller rig frame.

According to Figure 2 the degrees of freedom of the running gear are the four wheel rotations $\omega_{ms}$ with $m \in \{f, r\}$ for front ($f$) and rear ($r$) axle, and $s \in \{l, r\}$ for left ($l$) and right ($r$) wheel, the yaw motions of the wheel-carriers $\psi_m$ and the three rotational motions of the frame, i.e., the roll-angle $\alpha_F$, the pitch-angle $\beta_F$ and the yaw angle $\psi_F$. The vertical and lateral motions of the frame are represented by $z_F$, and $y_F$, respectively. The inertial system of the frame is denoted by the index $F$. The light gray area depicts the rear half of the running gear, which is not explicitly considered in the system description in Section 2. As a result the system description is reduced to a more manageable degree for our aim. For a detailed description see [7].

Figure 3 shows the schematic setup of the front wheel-pair of the running gear. Herein, one drive unit consists of the corresponding in-wheel motor, the integrated encoder sensor and one force-torque sensor (FTS). The FTS is an in-house product and is based on interconnected strain gauge system. The sensor signals of the FTS are transferred via RS-485 standard directly to the real-time unit. The running gear hardware is connected to a rapid control prototyping environment. The simulation models are implemented in *MATLAB / Simulink* and compiled via the *Simulink Real-Time* toolbox. With this toolbox a real time environment on a personal computer (PC) hardware is established. Except for the FTS, the sensor signals are transferred to the target PC over CAN bus (Control Area Network). As a control synthesis testbed the running gear

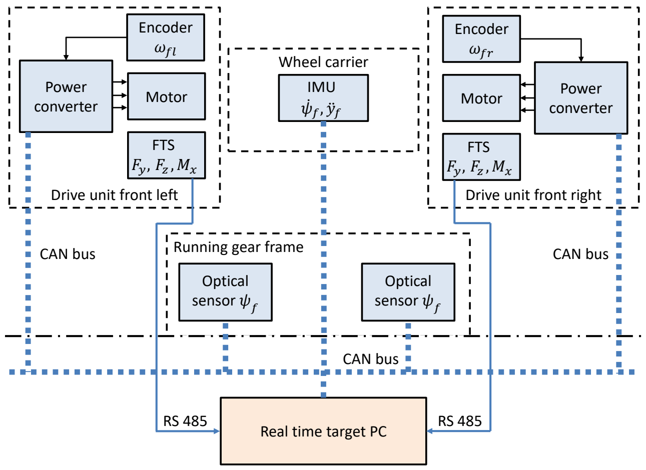

Figure 3: Schematic setup of the front wheel-pair.

on roller rig is equipped with sensors to measure the system states concerning the system dynamics. These measurement signals are the yaw angle $\psi_f$ of the wheel-carrier relative to the running gear frame which is measured by two optical sensors attached to the frame. By this configuration the pitch angle is compensated. In addition, the angular velocity $\omega_{ms}$ of each wheel is measured by its own absolute encoder. To measure the lateral position $y_F$ directly under laboratory conditions optical sensors are used. These sensors are attached to the roller rig frame and measure the lateral position $y_F$ as well as the yaw angle $\psi_F$ of the running gear frame. The configuration of the optical sensors to directly measure the lateral motion and the yaw angle is difficult to implement on a real track and is, therefore, only used on the testbed to validate the estimated lateral displacement. An indirect method to measure the lateral displacement is established by the use of FTSs. The FTSs couple the wheels to the axle bridges. Additionally, an IMU is integrated in each wheel-carrier. Each IMU consists of a gyroscope and an acceleration sensor to measure about and along the three axes in the wheel-carrier.

### *1.3. Problem definition*

The potential of a controlled lateral motion in combination with an observer for the running gear was shown in simulation studies, see [8]. The main message of the studies is that, a reliable estimation of the lateral position of the running gear is of crucial importance for the control of the lateral motion. Thus, in the previous work [1] the nonlinear system description was introduced and its observability for different sensor configurations was verified. Moreover, the suitability of each sensor configuration and system description for the design of an observer was a matter of subject. The observers were synthesized and used to compare simulation results and hardware measurements of the running gear. However, it was shown that the lateral dynamics of the running were not completely reproduced by the system description especially at sudden changing directions in the movements of the IRWs.

Therefore, it is the aim of this work to extend the system description with a nonlinear description of the wheel-rail geometry and to synthesize an appropriate observer to estimate the lateral position more reliably. For this purpose the running gear was equipped with a scaled S1002 wheel profile, following the DIN standard [9]. To increase the numerical precision of the herein applied extended Kalman filter the U-D filtering formulation following [10] is used.

Section 2 describes the equations of motion of the system and the chosen sensor configurations. Section 3 analyzes the structural observability of the nonlinear system. The observer design is presented in Section 4. The results of the observer design and the validation based on real measurements of the running gear are presented and discussed in Section 5. Section 6 concludes the paper and gives an outlook to future work.

## 2. System description

In the following, the equations of motion of the system derived in [1] are recalled and complemented by a nonlinear description of the wheel-rail geometry.

### *2.1. Running gear*

To validate and to enhance the control strategies that are developed in a simulation environment the running gear on the roller rig was developed. The accurate determination of the lateral position is of crucial importance for the control development. Therefore, the main emphasis here is on the development of a practical sensor concept in correspondence with an appropriate algorithm to accurately describe the displacement of the running gear. Regarding sensor and data fusion, the potential offered by model-based observer concepts is examined. For this purpose, a multibody model (MBM), see [11], and a nonlinear analytical model using *Modelica* of the running gear is developed and implemented [7].

Using the Euler-Lagrange formalism the equations of motion are derived as

$$\frac{\mathrm{d}}{\mathrm{d}t}\left(\frac{\partial T}{\partial \dot{\boldsymbol{q}}}\right)^{\mathrm{T}} - \left(\frac{\partial T}{\partial \boldsymbol{q}}\right)^{\mathrm{T}} + \left(\frac{\partial V}{\partial \boldsymbol{q}}\right)^{\mathrm{T}} = \boldsymbol{Q}_{fr} + \boldsymbol{Q}_{fl}, \qquad (1)$$

where $\boldsymbol{Q}_{fr}$ and $\boldsymbol{Q}_{fl}$ represent the generalized forces. Here, the time derivative $\dot{\boldsymbol{q}}$ of the generalized coordinates $\boldsymbol{q} = [y_f, \psi_f, \varphi_{fr}, \varphi_{fl}]^T$ and the kinetic and potential energy $T$ and $V$, respectively are presented. The time derivative of the rotation angles $\varphi_{fs}$ yields the respective angular velocity $\dot{\varphi}_{fs} = \omega_{fs}$. The kinetic and potential energy $T$ and $V$ depend also on the vertical displacement $z_f$ of the axle bridge and the roll-angle $\alpha_f$. The roll-angle can be expressed as

$$\alpha_f \approx \tan\alpha_f = -\frac{d}{\frac{b}{2} - r_0 d} y_f = -\Gamma y_f \qquad (2)$$

referring to the kinematic relation between the rotation of the axle bridges about the $x$-axis and their translation along the $y$-axis [6]. The vertical displacement of the wheel carrier mass $z_f$ is on the one hand characterized through the yaw motions of the axle bridges and on the other hand through their lateral displacements. These influences can be treated separately, see [6], so that the vertical displacements of the axle bridges are

$$z_f = z_{f,\psi_f} + z_{f,\alpha_f} = \frac{db}{2}\left(\frac{1}{\cos\psi_f} - 1\right) + y_f \tan\alpha_f. \qquad (3)$$

The roll-angle $\alpha_f$ and the vertical displacement $z_f$ are substituted into $T$ and $V$, respectively.

The calculation of the generalized forces is described for the right wheel in the following. The generalized force depends on the Jacobian of the absolute and angular velocities $\boldsymbol{v}_{fr}$ and $\boldsymbol{\Omega}_{fr}$ at the contact point of wheel and rail with respect to the generalized velocities

$$\boldsymbol{Q}_{fr} = \left(\frac{\partial \boldsymbol{v}_{fr}}{\partial \dot{\boldsymbol{q}}}\right)^T \boldsymbol{f}_{fr} + \left(\frac{\partial \boldsymbol{\Omega}_{fr}}{\partial \dot{\boldsymbol{q}}}\right)^{\mathrm{T}} \begin{pmatrix} 0 \\ \tau_f \\ 0 \end{pmatrix}. \tag{4}$$

The velocities

$$\boldsymbol{v}_{fr} = \boldsymbol{A}_{\psi I} \begin{pmatrix} 0 \\ \dot{y}_f \\ \dot{z}_f \end{pmatrix} + \left( \boldsymbol{\Omega}_{fr} \times \begin{pmatrix} x_{fr} \\ y_{fr} \\ r_{fs} \end{pmatrix} \right), \tag{5}$$

$$\boldsymbol{\Omega}_{fr} = \begin{pmatrix} 0 \\ \dot{y}_f \\ \dot{z}_f \end{pmatrix} + \begin{pmatrix} \cos\psi_f \dot{\alpha}_f \\ \sin\psi_f \dot{\alpha}_f \\ \dot{\psi}_f \end{pmatrix} \tag{6}$$

and the creep forces $\boldsymbol{f}_{fr}$ in the wheel-rail contact are deduced as suggested in [6]. Furthermore, Kalker's linear theory [12] is used to calculate the creep forces. The maximum creep force is limited to $f_{max} = F_N \mu$ with the normal wheel force $F_N$ and the friction coefficient $\mu$ between wheel and rail. To decrease the computational effort the creep torque is neglected according to [13] and the *Kalker* coefficients $C_{11}, C_{22}, C_{23}$ are kept constant. Therefore, the contact formulation

$$\boldsymbol{f}_{fr} = \begin{pmatrix} f_{x,fr} \\ f_{y,fr} \end{pmatrix} = \boldsymbol{K}_{Kal} \begin{pmatrix} s_{x,fr} \\ s_{y,fr} \\ \phi_{z,fr} \end{pmatrix} \tag{7}$$

with

$$\boldsymbol{K}_{Kal} = -ab_{fr} G \begin{pmatrix} C_{11} & 0 & 0 \\ 0 & C_{22} & \sqrt{ab_{fr}} C_{23} \end{pmatrix} \tag{8}$$

is considered as in [14]. Here, the longitudinal creep force $f_{x,fr}$, the lateral creep force $f_{y,fr}$, and the slip $\boldsymbol{s}_{fr} = [s_{x,fr}, s_{y,fr}, \phi_{z,fr}]^T$ with the longitudinal slip $s_{x,fr}$, the lateral slip $s_{y,fr}$, and the spin $\phi_{z,fr}$ are multiplied by the so-called Kalker matrix $\boldsymbol{K}_{Kal}$. In addition, the shear modulus $G$ and the Kalker coefficients, which depend on the product of the semi-axes contact ellipse $ab_{fr}$, see [15], are considered. The contact ellipse semi-axes used in (8) are calculated as

$$\sqrt{ab_{fr}} = \sqrt[3]{3 \frac{F_{N,fr}(1-\kappa_{Kal})E_g}{2\pi(A+D)G\sqrt{g_\nu}}} \tag{9}$$

according to [16]. They depend on the force $F_{N,fr}$ normal to the contact patch and the geometrical parameters $A$ and $D$, which are determined by the curvature of the contacting bodies in the vicinity of the contact patch. The variation of these parameters due to small yaw angles and lateral motions of the axle bridges is neglected. In the same way, the associated, dimensionless parameters $E_g$ and $g_\nu$ are set to a fixed value. The slip and spin of the nonlinear running gear model is formulated with the vector

$$\boldsymbol{s}_{fr} = \frac{1}{v_R} \begin{pmatrix} v_{x,fr} + v_R \cos\psi_f \\ v_{y,fr} - v_R \sin\psi_f \\ \Omega_{z,fr} \end{pmatrix}, \tag{10}$$

where the longitudinal roller velocity is represented by $v_R$. For a detailed explanation of the generalized forces and the system parameters, the reader is referred to [7].

### *2.2. Wheel-rail geometry*

The wheel-rail profile is approximated analogous to [17] for the test bench. One major nonlinearity of the railway system originates from the nonlinear wheel-rail profile. The profile standard used here is point-wise defined by [9] and corresponds to a conventional pairing S1002 / UIC60 wheel-rail profile. The rolling radius $r_{fs}$, which influences the creepage and therefore the contact forces, determines the system dynamics substantially. Another relevant value, which affects the direction of contact forces, is the contact angle $\delta_{0,fs}$. The rolling radius $r_{fs}$ and the contact angle $\delta_{0,fs}$ depend on the lateral position $y_f$. On the left side of Figure 4 the nonlinear wheel-rail geometry is sketched, where the dependencies of the rolling radius $r_{fs}$ and the contact angle $\delta_{0,fs}$ to the lateral position $y_f$ are shown. The right upper plot in Figure 4 shows the relationship between rolling radius and displacement and the right lower plot illustrates the contact angle over the lateral position. In both plots the results of the multibody simulation tool *Simpack* (black dashed line) and an approximation (blue line) in the relevant area $y_f = [-5, 5]$ mm is depicted. To give a continuous description of the wheel-rail geometry the data points from *Simpack* are fitted by exponential functions, which are simple to differentiate. Furthermore, the analytical description of the contact geometry makes it more convenient to handle in the system description without the need of look-up tables from the DIN standard in [9]. Continuous differentiability is a preliminary for the observability analysis which is in principle based on smooth vector fields and output functions, see Section 3. The approximated wheel-rail geometry in the form exponential functions is given by

$$\delta_{0,fs}(y_f) = \delta_1 e^{\pm\delta_2 y_f} + \delta_3 e^{\pm\delta_4 y_f} \tag{11}$$

$$r_{fs}(y_f) = r_1 + r_2 e^{\pm r_3 y_f} \tag{12}$$

with the corresponding fitted coefficients $r_i$, $i \in \{1,2,3\}$ and $\delta_j$, $j \in \{1,2,3,4\}$. The coefficients are derived by using the *Matlab Curve Fitting Toolbox* to fit the course of the S1002 profile geometry. Using these approximations of the contact angle and the rolling radius the creep forces

$$\begin{aligned} \boldsymbol{f}_{x,fr} = \frac{-Gab_{fr}C_{11}}{v_R+1} \Big[ & \dot{y}_f \psi_f - \frac{b}{2}\dot{\psi}_f + \omega_{fr} r_{fs} + y_f \Big( \dot{\psi}_f \\ & + \delta_{0,fr}\omega_{fr} \Big) + y_f r_{fs} \Gamma \left( \dot{\psi}_f + \delta_{0,fr}\omega_{fr} \right) + \dot{y}_f \psi_f r_{fs} \Gamma \Big] \end{aligned} \tag{13}$$

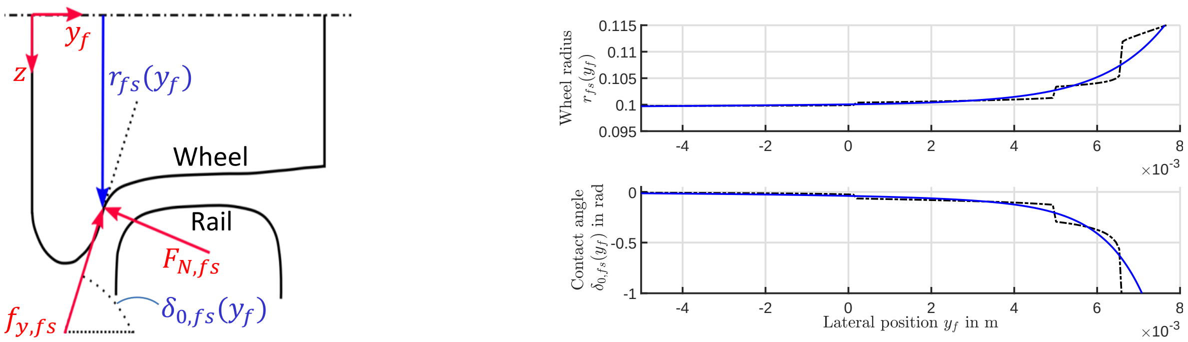

Figure 4: Nonlinear wheel-rail geometry (left) and approximations of wheel-rail geometry (right). Approximated wheel radius and contact angle (blue) by exponential functions (11) and (12) in comparison to *Simpack* results (black dashed line).

and

$$\boldsymbol{f}_{y,fr} = \frac{Gab_{fr}C_{22}}{v_R}\Bigg[\psi_f - \Bigg(\dot{y}_f + \Gamma\dot{y}_f r_{fs} + \Gamma\delta_{0,fr}\dot{y}_f y_f + \Gamma^2\delta_{0,fr}\dot{y}_f r_{fs} y_f + \frac{b}{2}\frac{\dot{\psi}_f\psi_f r_{fs}}{r_{fs} + r_R + \delta_{0,fr}y_f + \Gamma\delta_{0,fr}r_{fs}y_f}\Bigg)\Bigg] + \frac{Gab_{fr}^{3/2}C_{23}\left(\dot{\psi}_f + \delta_{0,fr}\left(\omega_{fr} + \Gamma\dot{y}_f\psi_f\right)\right)}{v_R} \tag{14}$$

can be formulated.

### 2.3. Equations of motion

In the present work the analytical model is expressed with the state vector $\boldsymbol{x} = [y_f, \dot{y}_f, \psi_f, \dot{\psi}_f, \omega_{fr}, \omega_{fl}]^{\mathrm{T}}$ and the input $u = \tau_f$ representing the differential torque between left and right wheel generated by the respective drive-units. The rotation angles $\varphi_{fs}$ of the wheels are not important for the state description in our case and are therefore not included in the analytical model. Substituting (4) in (1) and taking the definition of $\boldsymbol{x}$ into account yields a model description in the form

$$\begin{aligned} \dot{\boldsymbol{x}} &= \boldsymbol{a}(\boldsymbol{x}) + \boldsymbol{b}u, \\ g_i &= c_i(\boldsymbol{x}), \qquad i = 1, \ldots, p. \end{aligned} \tag{15}$$

Here $p$ denotes the number of system outputs. By assuming that the lateral velocity $\dot{y}_f$ is directly proportional to the yaw angle $\psi_f$ and the longitudinal speed $v_R$ according to

$$\dot{y}_f = \xi v_R \psi_f, \tag{16}$$

a reduced system description is established. Herein, $\xi = 1/(1+\Gamma r_0)$ is assumed to be a constant parameter depending on the wheel geometry. The parameter $\Gamma$ represents the relation between the contact angle, the wheel gauge $b$, and the nominal rolling radius $r_0$. As stated in [6], this assumption is only valid for low slip. Based on this a reduced system with five states $\boldsymbol{\zeta} = [y_f, \psi_f, \dot{\psi}_f, \omega_{fr}, \omega_{fl}]^{\mathrm{T}}$ is generated by eliminating the state $\dot{y}_f$ and is given schematically as

$$\dot{\boldsymbol{\zeta}} = \begin{bmatrix} \xi v_R \zeta_2 \\ \zeta_3 \\ a_4(\boldsymbol{\zeta}) \\ a_5(\boldsymbol{D}_5\boldsymbol{\zeta}) \\ a_6(\boldsymbol{D}_6\boldsymbol{\zeta}) \end{bmatrix} + \begin{bmatrix} 0 \\ 0 \\ 0 \\ 1/C \\ -1/C \end{bmatrix} \tau_f. \tag{17}$$

Herein, the matrices

$$\begin{aligned} \boldsymbol{D}_5 &= \operatorname{diag}(1,1,1,1,0), \\ \boldsymbol{D}_6 &= \operatorname{diag}(1,1,1,0,1) \end{aligned}$$

are used to extract the relevant states from the vector $\boldsymbol{\zeta}$.

### 2.4. Sensor configurations

Two sensor configurations are defined to assess the possible sensor signals needed to estimate the lateral displacement

$$_3\boldsymbol{g} = \left[\psi_f,\ \omega_{fr},\ \omega_{fl}\right]^{\mathrm{T}}, \tag{18}$$

$$_6\boldsymbol{g} = \left[\psi_f,\ \omega_{fr},\ \omega_{fl},\ \bar{F}_y,\ \bar{F}_z,\ \bar{M}_x\right]^{\mathrm{T}}. \tag{19}$$

These sensor configurations consist of realistic sensor signals, which can be measured in a real train with corresponding sensors. The low-level sensor configuration $_3\boldsymbol{g}$ is defined, consisting of the yaw angle $\psi_f$ and the rotational speeds $\omega_{fs}$ of the front wheel-pair. The high-level configuration $_6\boldsymbol{g}$ is generated through the combination of $_3\boldsymbol{g}$ and the FTS signals lateral force $\bar{F}_y$, vertical force $\bar{F}_z$, and torque $\bar{M}_x$ about the longitudinal axis. From a technical viewpoint the integration of the low-level setting into the other configuration represents a fallback level. If a failure in a sensor like the FTS in $_6\boldsymbol{g}$ occurs, the estimation of the position is still ensured. In case malfunctioning or total breakdown of the FTS, the general operation of the running gear is not at risk but would require to reduce the travel speed of the train.

The configuration $_3\boldsymbol{g}$ provides the lateral position at lower accuracy compared to $_6\boldsymbol{g}$, see Table 1. Even with lower accuracy, the low-level sensor configuration is appealing from an economic point of view. The results in

Table 1 rely on the equation to calculate the contact point of one wheel

$$y_{fs} = \frac{rF_{y,fs} - a_R F_{z,fs} + M_{x,fs} + gM_R y_{cg}}{F_{z,fs} + gM_R}. \tag{20}$$

Equation 20 is derived from the moment equilibrium around the contact between wheel and rail and the connection of the FTS to the axle bridge [2]. The moment equilibrium is depicted in Figure 5. Where the gravity constant is denoted with $g$ and the mass of one wheel is specified by $M_R$. The distance from the nominal wheel radius $r_0$ to the measuring plane of the FTS is denoted by $a_R$ and the distance from $r_0$ to the center of gravity of the wheel mass is described by $y_{cg}$. By inserting the measurement equations (28), (29) and (30) into (20) and by applying error propagation the accuracy of each sensor configuration, in Table 1, is calculated.

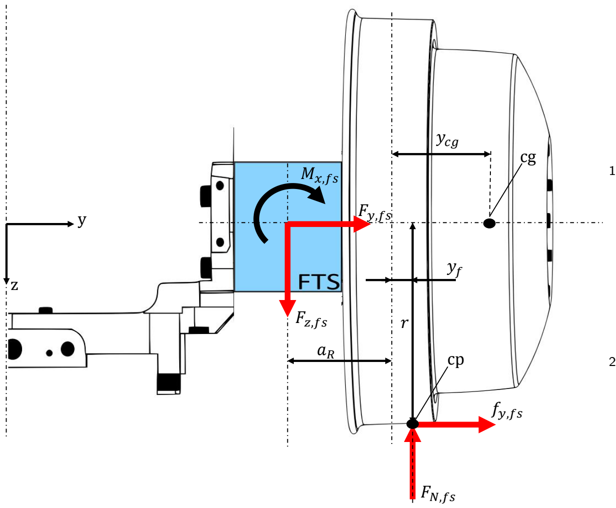

Figure 5: Moment equilibrium around the contact point and the FTS.

| Sensor configuration | Error tolerance |
|---|---|
| $_3\boldsymbol{g}$ | $\approx 5 \times 10^{-4}$ |
| $_6\boldsymbol{g}$ | $\approx 1.2 \times 10^{-4}$ |

Table 1: Accuracies of the lateral displacement estimation.

## 3. Nonlinear observability analysis

In order to create the basis for a reliable observer and thus a safe system for determining the lateral position, the observability of the models determined in Section 2 are analyzed here. The observability analysis is adopted from [1] .

### 3.1. Uniform observability analysis

A general output vector $\boldsymbol{g} = [g_1, \dots, g_p]^{\mathrm{T}}$ is denoted for the autonomous system $\dot{\boldsymbol{x}} = \boldsymbol{a}(\boldsymbol{x})$ given $u = 0$ . By making use of successive Lie derivatives for each output component $g_i$ the vector

$$\boldsymbol{z}_i = \left[g_i, L_{\boldsymbol{a}} g_i, \dots, L_{\boldsymbol{a}}^{n_i - 1} g_i\right]^{\mathrm{T}} \tag{21}$$

is generated. Combination of $\boldsymbol{z}_i$ for each $i = 1, 2, \dots, p$ yields the observability mapping

$$\boldsymbol{z} = \begin{bmatrix} \boldsymbol{z}_1 \\ \vdots \\ \boldsymbol{z}_p \end{bmatrix} = \boldsymbol{h}(\boldsymbol{x}) \quad \text{with} \quad \sum_{i=1}^{p} n_i = n. \tag{22}$$

The system is called uniformly observable, if $\boldsymbol{h}^{-1}(\boldsymbol{z})$ exists globally and locally observable, if the inverse exists only in a neighborhood of a given $\boldsymbol{x}$, see [18, 19]. Subsequently, this approach is applied to the systems (15) and (17) with the two sensor configurations defined in (18) and (19).

### 3.2. Observability of the low slip system

For the reduced system the observability mapping $\boldsymbol{h}(\boldsymbol{\zeta})$ (17) with the sensor setting $_3\boldsymbol{g}$ is formed as

$$\boldsymbol{z} = \boldsymbol{h}_\zeta(\boldsymbol{\zeta}) = \begin{bmatrix} \boldsymbol{z}_1 \\ \hline z_2 \\ z_3 \end{bmatrix} = \begin{bmatrix} \zeta_2 \\ \zeta_3 \\ a_4(\boldsymbol{\zeta}) \\ \hline \zeta_4 \\ \zeta_5 \end{bmatrix}. \tag{23}$$

The element $a_4(\boldsymbol{\zeta})$ of the right hand side vector field can be solved for $\zeta_1$ explicitly for the reduced system (17). The system (23) is locally observable with $_3\boldsymbol{g}$ due to the existence of the inverse $\boldsymbol{\zeta} = \boldsymbol{h}_\zeta^{-1}(\boldsymbol{z})$ for $v_R \neq 0$ (due to the slip model). The local observability of the low-level configuration $_3\boldsymbol{g}$ carries over to the high-level sensor configuration $_6\boldsymbol{g}$ under low slip conditions.

### 3.3. Observability of the full order system

For high acceleration and deceleration processes in which high slip conditions appear the system (17) may not be valid. For this reason, the observability of the full order system is analyzed due to the restrictions imposed by the assumption (16) for the reduced system.

The dependencies of the right hand side of the full order system description (15) can be schematically shown as

$$\dot{\boldsymbol{x}} = \begin{bmatrix} \dot{y}_f \\ a_2(y_f, \dot{y}_f, \psi_f, \dot{\psi}_f, \omega_{fr}, \omega_{fl}) \\ \dot{\psi}_f \\ a_4(y_f, \dot{y}_f, \psi_f, \dot{\psi}_f, \omega_{fr}, \omega_{fl}) \\ a_5(y_f, \dot{y}_f, \psi_f, \dot{\psi}_f, \omega_{fr}) \\ a_6(y_f, \dot{y}_f, \psi_f, \dot{\psi}_f, \omega_{fl}) \end{bmatrix} + \begin{bmatrix} 0 \\ 0 \\ 0 \\ 0 \\ 1/C \\ -1/C \end{bmatrix} \tau_f, \tag{24}$$

where the equations $a_2$, $a_5$ and $a_6$ are not provided due to their complexity. The yaw-motion of the full order system is specified as

$$\begin{aligned}a_4(\boldsymbol{x}) =& \frac{\vartheta_7\Big(Gab_{fr}C_{22}\vartheta_5 + Gab_{fr}{}^{3/2}C_{23}\vartheta_3\Big)}{B} - \frac{\kappa\psi_f}{B}\\ &- \frac{\vartheta_8\Big(Gab_{fl}C_{22}\vartheta_6 + Gab_{fl}{}^{3/2}C_{23}\vartheta_4\Big)}{B}\\ &- \frac{Gab_{fl}C_{11}\vartheta_2\big(\frac{b}{2} + \xi y_f\big)}{B}\\ &+ \frac{Gab_{fr}C_{11}\vartheta_1\big(\frac{b}{2} - \xi y_f\big)}{B},\end{aligned} \tag{25}$$

with the yaw stiffness $\kappa$ between wheel pair and frame and the moment of inertia $B$ of the wheel carrier around its vertical axis. The substitutions $\vartheta_i$ can be found in the appendix, for the sake of completeness. The component $a_4(\boldsymbol{x})$ can be solved for $x_1 = y_f$, taking the system description of the full order system (15) with the sensor configuration (18) into account. However, there is not only one solution to determine $y_f$ from $a_4(\boldsymbol{x})$. Nevertheless, for the condition $v_R \neq 0$ an appropriate inverse function $\boldsymbol{h}^{-1}_{3\boldsymbol{g}}(\boldsymbol{z})$ can be formulated, so that the system is considered to be locally observable.

Proceeding similarly for ${}_6\boldsymbol{g}$ defined in (19) in view of the system equations (15) yields

$$\boldsymbol{z} = \boldsymbol{h}_{6\boldsymbol{g}}(\boldsymbol{x}) = \begin{bmatrix} x_3\\ x_5\\ x_6\\ \bar{F}_y(\boldsymbol{x})\\ \bar{F}_z(\boldsymbol{x})\\ \bar{M}_x(\boldsymbol{x})\end{bmatrix} \tag{26}$$

with the forces $\bar{F}_y$, $\bar{F}_z$ and the torque $\bar{M}_x$ are basically representing the arithmetic mean of the particular forces and torque of one wheel-pair

$$\begin{aligned}\bar{F}_y &= \frac{1}{2}\left(F_{y,fr} + F_{y,fl}\right),\\ \bar{F}_z &= \frac{1}{2}\left(F_{z,fr} + F_{z,fl}\right),\\ \bar{M}_x &= \frac{1}{2}\left(M_{x,fr} + M_{x,fl}\right).\end{aligned} \tag{27}$$

The measurement equation for the lateral force in the contact patch is described by

$$\begin{aligned}F_{y,fs}(\boldsymbol{x}) = \delta_{0,fs}\left(\sigma_4 - \sigma_3\right) - \sigma_{10} + \sigma_{11}\\ + \Gamma g M_R y_f + \sigma_2 - \sigma_1,\end{aligned} \tag{28}$$

the equation for the vertical force reads

$$F_{z,fs}(\boldsymbol{x}) = \sigma_3 + \sigma_4 - \delta_{0,fs}(\sigma_{10} + \sigma_{11} + \sigma_1 + \sigma_2), \tag{29}$$

and the torque about the longitudinal axis is given by

$$\begin{aligned}M_{x,fs}(\boldsymbol{x}) = &(\sigma_{10} + \sigma_1)(\sigma_5 + l_g\delta_{0,fs} - \sigma_9)\\ &+ (\sigma_{11} + \sigma_2)(\sigma_5 - l_g\delta_{0,fs} + \sigma_9)\\ &- gM_R l_R - \sigma_4(\sigma_6 + \delta_{0,fs}r_{fs} - l_g)\\ &- \sigma_3(\sigma_6 - \delta_{0,fs}r_{fs} + l_g).\end{aligned} \tag{30}$$

The measurement equations of the FTS in (28)-(30) are generated by geometric relations and applied contact mechanics, see Figure 5. The expressions subsummed in $\sigma_i$ are summarized in the appendix. Under the assumption that $v_R \neq 0$ and by directly measuring the state components $x_3 = \psi_f$, $x_5 = \omega_{fr}$, and $x_6 = \omega_{fl}$ the state $x_1 = y_f$ can be reconstructed from $\bar{F}_y(\boldsymbol{x})$ in (28). The states $x_2 = \dot{y}_f$ and $x_4 = \dot{\psi}_f$ can be determined from (29) and (30), respectively. Thus, the full order system with the high-level sensor configuration ${}_6\boldsymbol{g}$ can be considered locally observable .

## 4. Observer synthesis

It has been shown in [1] that the extended Kalman filter (EKF) provides an appropriate observer to estimate the lateral position of the nonlinear systems. However, occasionally during operation of the testbed the conservative EKF algorithm has shown deficiency in numerical precision. Therefore, in this work an alternate EKF formulation namely U-D filtering is chosen. The U-D algorithm introduced in [10] increases the numerical precision with the side effect to increase the computational cost but not as severely as the square root filtering, see [20].

### *4.1. Extended Kalman filter*

The standard EKF algorithm regards a discrete-time nonlinear dynamic system with additive Gaussian noise. The process noise $\boldsymbol{\varepsilon} \sim \mathcal{N}(\boldsymbol{0}, \boldsymbol{Q})$ and measurement noise $\boldsymbol{\delta} \sim \mathcal{N}(\boldsymbol{0}, \boldsymbol{R})$ with the respective covariance matrices $\boldsymbol{Q}$ and $\boldsymbol{R}$, are assumed of zero mean. The EKF expects the states to be Gaussian distributed. This distribution is propagated through the first order linearization of the nonlinear system.

By using a third order Runge-Kutta scheme to discretize the system (15) the representation $\boldsymbol{a}_{k|k-1}$ is formulated and the discrete time version is formulated by

$$\begin{aligned}\boldsymbol{x}_k &= \boldsymbol{a}_{k|k-1}(\boldsymbol{x}_{k-1}, u_{k-1}) + \boldsymbol{\varepsilon}_{k-1},\\ \boldsymbol{g}_k &= \boldsymbol{c}(\boldsymbol{x}_k) + \boldsymbol{\delta}_k,\end{aligned} \tag{31}$$

with $t_k$ as the $k$-th sample time instant of a periodically sampled data system, $\boldsymbol{x}_k = \boldsymbol{x}(k)$, $\boldsymbol{g}_k = \boldsymbol{g}(k)$. The prediction step of the EKF algorithm is given as

$$\hat{\boldsymbol{x}}_k^- = \boldsymbol{a}_{k|k-1}(\hat{\boldsymbol{x}}_{k-1}, u_{k-1}), \tag{32}$$

$$\boldsymbol{P}_k^- = \boldsymbol{A}_k\boldsymbol{P}_k\boldsymbol{A}_k^{\mathrm{T}} + \boldsymbol{Q}. \tag{33}$$

Where $\boldsymbol{A}_k$ represents the Jacobian of the discrete system $\boldsymbol{a}_{k|k-1}$ at $\boldsymbol{x} = \hat{\boldsymbol{x}}_{k-1}$. To correct the estimation of state vector $\hat{\boldsymbol{x}}_k$ and the state covariance matrix $\boldsymbol{P}_k$ the Kalman gain $\boldsymbol{K}_k$ is used and the correction step cas be formulated as

$$\boldsymbol{K}_k = \boldsymbol{P}_k^-\boldsymbol{H}_k^{\mathrm{T}}\left(\boldsymbol{H}_k\boldsymbol{P}_k^-\boldsymbol{H}_k^{\mathrm{T}} + \boldsymbol{R}\right)^{-1}, \tag{34}$$

$$\hat{\boldsymbol{x}}_k = \hat{\boldsymbol{x}}_k^- + \boldsymbol{K}_k\left[\boldsymbol{g}_k - \hat{\boldsymbol{g}}_k^-\right], \tag{35}$$

$$\boldsymbol{P}_k = (\boldsymbol{I} - \boldsymbol{K}_k\boldsymbol{H}_k)\boldsymbol{P}_k^-. \tag{36}$$

The Jacobian $\boldsymbol{H}_k$ of the measurement function at $\boldsymbol{x} = \hat{\boldsymbol{x}}_k^-$ is required to correct the state estimation from the prediction step.

### *4.2. U-D filtering*

In the U-D filtering formulation the $n \times n$ matrix $\boldsymbol{P}$ is factorized as $\boldsymbol{U}\boldsymbol{D}\boldsymbol{U}^T$, where $\boldsymbol{U}$ is an $n \times n$ upper triangular matrix with ones along the diagonal and $\boldsymbol{D}$ is an $n \times n$ diagonal matrix. This is always true for a symmetric positive definite matrix $\boldsymbol{P}$ and as such can be implemented in a Kalman filter. Equations (34) and (36) are combined to the measurement update equation

$$\boldsymbol{P}_i = \boldsymbol{P}_{i-1} - \boldsymbol{P}_{i-1}\boldsymbol{H}_i^{\mathrm{T}} \left(\boldsymbol{H}_i\boldsymbol{P}_{i-1}\boldsymbol{H}_i^{\mathrm{T}} + R_i\right)^{-1} \boldsymbol{H}_i\boldsymbol{P}_{i-1} \tag{37}$$

at the correction step, where $\boldsymbol{H}_i$ is the $i$th row of $\boldsymbol{H}$, $R_i$ is the $i$th diagonal entry of $\boldsymbol{R}$, and $\boldsymbol{P}_i$ is the estimation covariance after $i$ measurements. With the definition of the scalar

$$\alpha_i := \boldsymbol{H}_i\boldsymbol{P}_{i-1}\boldsymbol{H}_i^{\mathrm{T}} + R_i, \tag{38}$$

and the assumptions

$$\boldsymbol{P}_{i-1} = \boldsymbol{U}_{i-1}\boldsymbol{D}_{i-1}\boldsymbol{U}_{i-1}^{\mathrm{T}}, \quad \boldsymbol{P}_i = \boldsymbol{U}_i\boldsymbol{D}_i\boldsymbol{U}_i^{\mathrm{T}} \tag{39}$$

if $\boldsymbol{P}_{i-1}$ and $\boldsymbol{P}_i$ are symmetric positive definite a U-D factorization is possible. The derivation of the matrices $\boldsymbol{U}_i$ and $\boldsymbol{D}_i$ can be found in [10] and is here briefly summarized in view of the considered application. The U-D factors are given by

$$\boldsymbol{U}_i\boldsymbol{D}_i\boldsymbol{U}_i^{\mathrm{T}} = \left(\boldsymbol{U}_{i-1}\bar{\boldsymbol{U}}_i\right) \bar{\boldsymbol{D}} \left(\boldsymbol{U}_{i-1}\bar{\boldsymbol{U}}_i\right)^{\mathrm{T}} \tag{40}$$

and

$$\begin{aligned} &\bar{\boldsymbol{U}}\bar{\boldsymbol{D}}\bar{\boldsymbol{U}}^{\mathrm{T}} = \\ &\left[\boldsymbol{D}_{i-1} - \frac{1}{\alpha_i}\left(\boldsymbol{D}_{i-1}\boldsymbol{U}_{i-1}^{\mathrm{T}}\boldsymbol{H}_i^{\mathrm{T}}\right)\left(\boldsymbol{D}_{i-1}\boldsymbol{U}_{i-1}^{\mathrm{T}}\boldsymbol{H}_i^{\mathrm{T}}\right)^{\mathrm{T}}\right]. \end{aligned} \tag{41}$$

In short this means that

$$\boldsymbol{U}_i = \boldsymbol{U}_{i-1}\bar{\boldsymbol{U}}_i \tag{42}$$

$$\boldsymbol{D}_i = \bar{\boldsymbol{D}}, \tag{43}$$

where $\boldsymbol{U}_{i-1}\bar{\boldsymbol{U}}_i$ is an upper triangular matrix with diagonal elements equal to 1, and $\bar{\boldsymbol{D}}$ is a diagonal matrix. The time-update equation for the covariance of the U-D filtering necessary for the prediction step of the Kalman filter algorithm is derived from (33) and can be written as

$$\begin{aligned} \boldsymbol{P}^- &= \boldsymbol{A}\boldsymbol{P}^+\boldsymbol{A}^{\mathrm{T}} + \boldsymbol{Q} \\ &= \begin{bmatrix}\boldsymbol{A}\boldsymbol{U}^+ & \boldsymbol{I}\end{bmatrix} \begin{bmatrix}\boldsymbol{D}^+ & 0 \\ 0 & \boldsymbol{Q}\end{bmatrix} \begin{bmatrix}\boldsymbol{U}^{+\mathrm{T}}\boldsymbol{A}^{\mathrm{T}} \\ \boldsymbol{I}\end{bmatrix} \\ &= \boldsymbol{W}\hat{\boldsymbol{D}}\boldsymbol{W}^{\mathrm{T}}, \end{aligned} \tag{44}$$

supposing that $\boldsymbol{P}^+$ is generated as $\boldsymbol{U}^+\boldsymbol{D}^+\boldsymbol{U}^{+\mathrm{T}}$ from the equations above and under the assumption

$$\boldsymbol{P}^- = \boldsymbol{U}^-\boldsymbol{D}^-\boldsymbol{U}^{-\mathrm{T}} \tag{45}$$

to find the U-D factors. Here $\boldsymbol{P}^-$ represents the state covariance matrix and $\boldsymbol{U}^-\boldsymbol{D}^-$ the U-D factors in the prediction step. Note that $\boldsymbol{W}$ is an $n \times 2n$ matrix and $\hat{\boldsymbol{D}}$ is a $2n \times 2n$ matrix. With the matrix $\boldsymbol{W}^{\mathrm{T}} = \left[\boldsymbol{w}_1^{\mathrm{T}} \cdots \boldsymbol{w}_n^{\mathrm{T}}\right]$ and $\boldsymbol{v}_k\hat{\boldsymbol{D}}\boldsymbol{v}_j^{\mathrm{T}} = 0$ for $k \neq j$, where $\boldsymbol{w}_i$ and $\boldsymbol{v}_i$ are $2n$-element row vectors and can be found with the Gram-Schmidt orthogonalization procedure, see [21], as

$$\boldsymbol{w}_k = \boldsymbol{v}_k + \sum_{j=k+1}^{n} \boldsymbol{u}(k,j)\boldsymbol{v}_j \quad k = 1, \cdots, n. \tag{46}$$

By this the definition of $\boldsymbol{u}(k,j)$ follows

$$\boldsymbol{u}(k,j) = \frac{\boldsymbol{w}_k\hat{\boldsymbol{D}}\boldsymbol{v}_j^{\mathrm{T}}}{\boldsymbol{v}_j\hat{\boldsymbol{D}}\boldsymbol{v}_j^{\mathrm{T}}} \quad j,k \in \{1, \cdots, n\} \tag{47}$$

and the calculation of $\boldsymbol{W}$ can be written as

$$\begin{bmatrix}\boldsymbol{w}_1 \\ \boldsymbol{w}_2 \\ \vdots \\ \boldsymbol{w}_n\end{bmatrix} = \begin{bmatrix}1 & \boldsymbol{u}(1,2) & \cdots & \boldsymbol{u}(1,n) \\ 0 & 1 & \ddots & \vdots \\ \vdots & \ddots & \ddots & \boldsymbol{u}(n-1,n) \\ 0 & \cdots & 0 & 1\end{bmatrix} \begin{bmatrix}\boldsymbol{v}_1 \\ \boldsymbol{v}_2 \\ \vdots \\ \boldsymbol{v}_n\end{bmatrix}$$

or, respectively,

$$\boldsymbol{W} = \boldsymbol{U}^-\boldsymbol{V}, \tag{48}$$

where $\boldsymbol{V}$ is a $n \times 2n$ matrix. Finally, the matrix product can be written as

$$\boldsymbol{W}\hat{\boldsymbol{D}}\boldsymbol{W}^{\mathrm{T}} = \boldsymbol{U}^-\boldsymbol{D}^-\boldsymbol{U}^{-\mathrm{T}} \tag{49}$$

to calculate the estimation covariance in the prediction step and the U-D factors can be determined by (48) and

$$\begin{aligned} \boldsymbol{D}^- &= \boldsymbol{V}\hat{\boldsymbol{D}}\boldsymbol{V}^{\mathrm{T}} = \mathrm{diag}(d_1, \cdots, d_n) \\ d_k &= \boldsymbol{v}_k\hat{\boldsymbol{D}}\boldsymbol{v}_k^{\mathrm{T}}. \end{aligned} \tag{50}$$

The extended Kalman filter with the U-D formalism is two times more precise than the standard EKF, just like the square root filter [22], but it requires less computational effort compared to the square root filter. Note that a sequential Kalman filter needs a diagonal and or constant measurement noise covariance matrix $\boldsymbol{R}$.

### *4.3. Optimization of covariances*

To design an appropriate estimator the covariance matrices of the process noise $\boldsymbol{Q}$ and measurement noise $\boldsymbol{R}$ need to be configured. A correct design of the covariance matrices ensures the convergence of the estimation error of the observers. Hence, the covariance matrices of the observers are optimized with the objective to minimize the error integral of the absolute difference between the measured lateral position $y_f$ and the estimated displacement $\hat{y}_f$. The software MOPS (Multi-Objective Parameter Synthesis) in *Simulink*, see [23], is used to configure $\boldsymbol{Q}$ and $\boldsymbol{R}$ for 27 measurements of motion scenarios of the running gear. For each optimization case $j \in S$ the decision variables $\boldsymbol{\rho} = ([\mathrm{diag}(\boldsymbol{Q}), \mathrm{diag}(\boldsymbol{R})])$ are subject to the constraints $10^{-6} \leq \rho_i \leq 100$. The aim of the optimization is to get an ideal parameter set defined in $\boldsymbol{\rho}$ which fulfills the criterion $o = \int |y_f - \hat{y}_f| \,\mathrm{d}t$ for each optimization case. The demand value $d$ ensures that $\max(o_j(\boldsymbol{\rho})) \leq d$, i.e. the maximum estimation error lies within a specific boundary for each optimization case. The general multi-case optimization problem is stated as

$$\min_{\boldsymbol{\rho}} \max_{j \in S} o_j(\boldsymbol{\rho}). \tag{51}$$

The number of decision variables $\boldsymbol{\rho}$ is adjusted with regard to the considered system (reduced or full order) and a corresponding sensor configuration. For each motion scenario of $S$ a set of parameters determines the movement of the running gear. A reference trajectory

$$Y_{wS} = y_S \sin(2\pi f_S t), \tag{52}$$

which describes a sinusoidal movement is provided for the lateral controller. Equation (52) represents the natural hunting motion of a conventional wheel-set. Note, that the running gear with IRW is a-priori unstable and therefore a feedback controller to applies the demanding motion scenario. The parameters of the motion scenarios used in the optimization cases are shown in Table 2. In accordance to the angular velocity $\omega_{ms}$, lateral displacement $y_S$ and the motion frequency $f_S$ with the chosen frequencies $f_h \in \{0.1, 0.3, 0.5\}$ Hz the optimization scenarios are distinguished.

| $\omega_{ms}$ in min$^{-1}$ | 100 | | | 150 | | | 200 | | |
|---|---|---|---|---|---|---|---|---|---|
| $y_S$ in mm | 1 | 3 | 5 | 1 | 3 | 5 | 1 | 3 | 5 |
| $f_S$ in Hz | $f_h$ | $f_h$ | $f_h$ | $f_h$ | $f_h$ | $f_h$ | $f_h$ | $f_h$ | $f_h$ |

Table 2: Optimization szenarios.

## 5. Results

This section presents the results of the optimization process to design the covariance matrices of the EKF with the U-D formalism. Furthermore, the designed observers are implemented on the real-time control system of the running gear to validate the estimation of the lateral position. The measured data is shown and discussed. The results for the estimated lateral position using the reduced model (17) and the full order model (15) with both sensor configurations (18) and (19) for chosen motion scenarios of the running gear are shown and discussed.

The following data was measured with a sample time $T_S = 200$ Hz. Furthermore, to reduce signal noise, the measured signals contained in the sensor configurations ${}_3\boldsymbol{g}$ and ${}_6\boldsymbol{g}$ are low-pass filtered with the cutoff frequency $f_e = 10$ Hz. The cutoff is based on the common assumption from real wheel-rail application, that frequencies above $f_{co} = 20$ Hz are of minor interest to the dynamics of a running gear. In accordance with the similarity laws from [6] the cutoff is scaled by the factor $\iota = 1/\sqrt{5}$, which yields $f_e = f_{co}/\iota$.

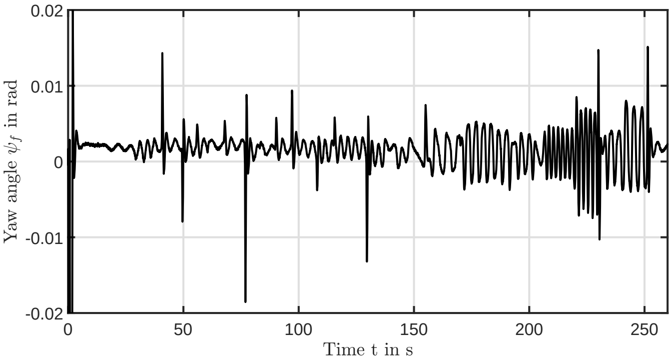

Figure 6: Measurement of yaw angle.

The measured yaw angle is shown in Figure 6. To avoid repetition, the measured angular velocities $\omega_{ms}$ are not shown as they mainly correspond to the velocity depicted in Figure 7c. Relatively high peaks of the $\psi_f$ at approximately $t \in \{45, 50, 75, 130, 230, 25\}$ s are visible. These high amplitudes correspond to the sudden changes of the lateral position in Figure 7a. Figure 7a shows estimation results based on the reduced model (17) from real measurements of the running gear. The scenario covers a mixed motion consisting of different constant lateral positions and different sinusoidal displacements. The estimation error of the measurement and estimation above is illustrated in Figure 7b. Herein, the estimation error is depicted in percentage, which lies mainly under 2.5 %. The estimation errors are calculated with respect to the direct measurement of the lateral position via optical sensors and the corresponding estimation of the observer based on the reduced model (17) In Figure 7c the measured speed of the wheels in longitudinal direction is depicted. It can be seen that the velocity varies over the course of the measurement. It is worth to mention, that a direct correlation between the changing velocity and the estimation error can not be determined. The estimation error seems to be higher at sudden changes of the lateral position such as in jumps of the displacement as well as in high frequent sinusoidal motions.

In Figure 8a the estimation results based on the full order model are shown. Here, the estimation error, from Figure 8b lies below 1 % with the low-level sensor configuration and overall lower than 0.5 % with the high-level sensor configuration. The velocity profile of these measurements is equal to Figure 7c. Just as in the measurements from the Figures 7b and 7b there is no noticeable link-

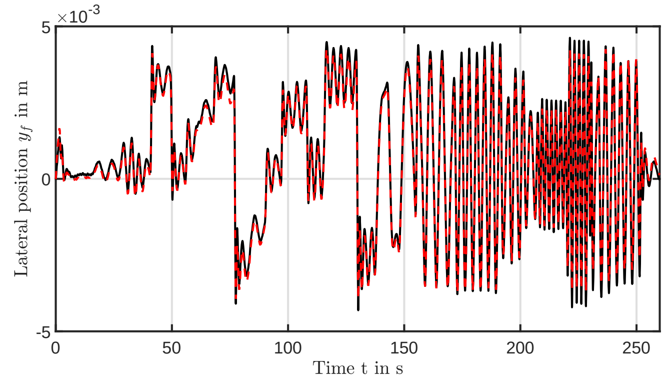

(a) Estimation results for reduced model observer settings. The measurement is represented by the black line and the estimation by the dashed red line.

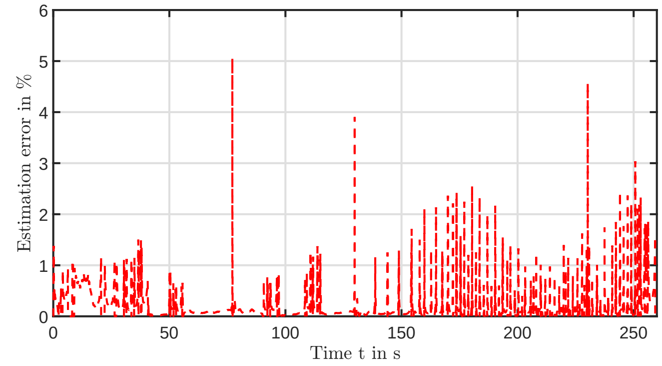

(b) Estimation error with the observer based on the reduced model.

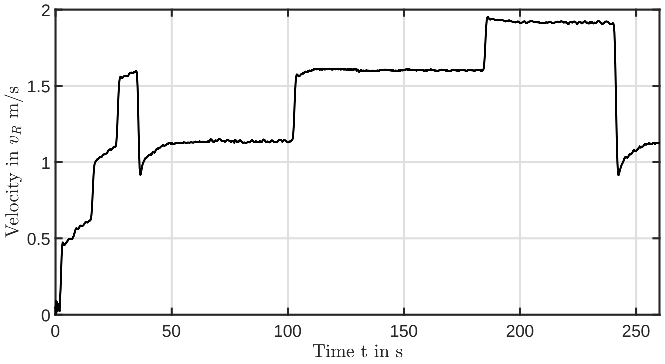

(c) Velocity profile from the measurement shown in Figures 7a and 8a.

Figure 7: Results for reduced model observer settings.

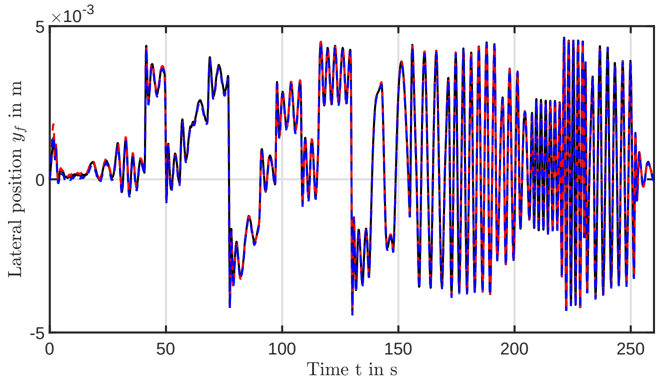

(a) Estimation based on full order model (15) with low-level ${}_3\boldsymbol{g}$ and high-level sensor configuration ${}_6\boldsymbol{g}$ represented by the dashed red and blue line, respectively.

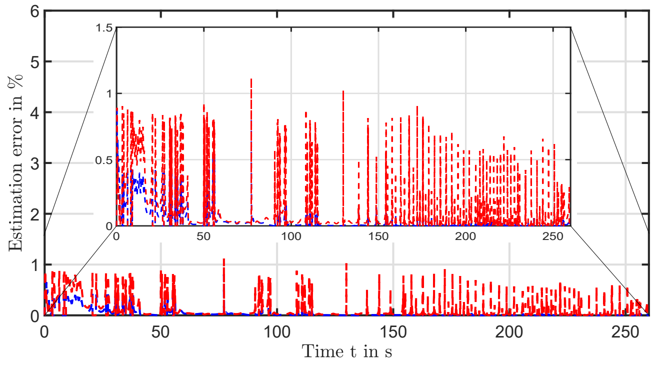

(b) Estimation error based on full order model (15) with low-level ${}_3\boldsymbol{g}$ and high-level sensor configuration ${}_6\boldsymbol{g}$ represented by the dashed red and blue line, respectively.

Figure 8: Results for full order model observer settings.

age between velocity and estimation error. Nevertheless, sudden changes of the lateral position of the real system visibly raise the estimation error. The estimations with the low-level sensor configuration are based on the measured signals of the yaw angle $\psi_f$ shown in Figure 6 and for the high-level setup in addition on the measurement of the FTS sensors in Figure 9. According to 27, the measurements are averaged. In the diagrams the signals are scaled with respect to their particular mean value. In the range $t \in [150, 260]$ s the vertical force $\bar{F}_z$ in Figure 9a shows similar characteristics to the lateral position from Figure 8a. Note, over the course of this motion scenario the relative change of $\Delta\bar{F}_z \approx \pm 5\,\%$. However, the overall relative change of the lateral force, in Figure 9b, amounts to $\Delta\bar{F}_y \approx \pm 20\,\%$. Furthermore, the qualitative lateral movement can be deduced better than from the vertical force in Figure 9a. Figure 9 shows the measured torque about the longitudinal axis corresponding to the movement scenario. Similar to the measurement of $\bar{F}_y$ the characteristic of the movement can be deduced, though not as accurate. Additionally, compared to $\Delta\bar{F}_y$ the overall relative change of the torque is higher with $\Delta\bar{M}_x \approx \pm 50\%$. The impact of high sudden changes of the lateral position is reflected by prominent peaks at $t \in \{45, 75, 130\}$ s contrary to the measurements of $\bar{F}_z$ and $\bar{F}_y$. The measurements in Figure 9 show that the qualitative movement of the running gear in the form of the lateral displacement can be reflected via the FTS. This explains the higher estimation accuracy of the ${}_6\boldsymbol{g}$ sensor configuration compared to the low-level setup ${}_3\boldsymbol{g}$. Due to the better reproduction of the movement characteristics, it seems reasonable that the lateral force $\bar{F}_y$ and the torque $\bar{M}_x$ have a greater impact on the estimation accuracy than the vertical force $\bar{F}_z$.

Figure 10a shows a demanding sinusoidal motion of the running gear with an increasing velocity in the range $v_R \in [0, 4]\frac{m}{s}$, shown in Figure 10c. The change of the

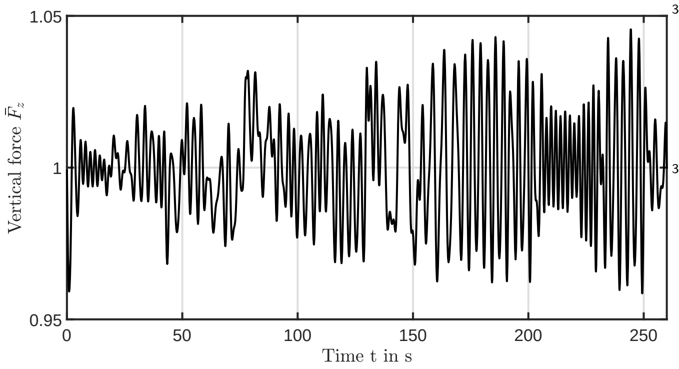

(a) Measured normed vertical force $\bar{F}_z$.

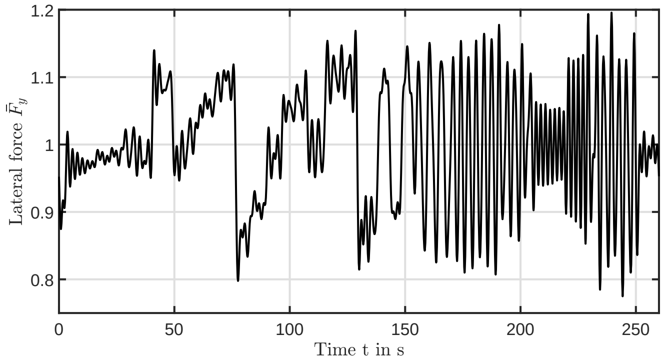

(b) Measured normed lateral force $\bar{F}_y$.

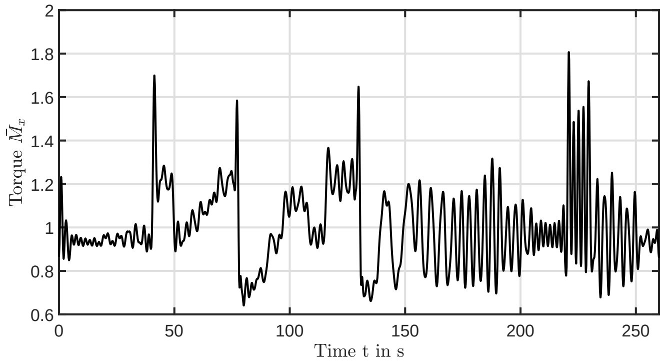

(c) Measured normed torque about the $x$-axis $\bar{M}_x$.

Figure 9: Measured normed signals by FTS for the estimations based on the full order system with the low-level ${}_3\boldsymbol{g}$ and high-level sensor configuration ${}_6\boldsymbol{g}$.

velocity occurs stepwise. From 50s onward an unstable behavior of the running gear can be seen which becomes more pronounced with increasing speed. At about 102s, the first contact of the contact flange with the rail can be seen in Figure 10a. The overall accuracy in percent lies below 2 % as shown in Figure 10c. It should be noted, that the observer is able to estimate the lateral position despite wheel flange contact, in which a double contact patch between flange and rail occurs. This double contact is not considered in the model description. At this point it should be highlighted that at this particular time of the running gear operation, the rotary drive for simulating the longitudinal speed is initiated by the rollers. Therefore, higher estimation errors can occur at rapidly rising speed, high slip situations, probably because of the changing roller velocity due to a yaw angle which differs from zero and as such results in an accelerated lateral velocity and hereby causing a sudden change in the lateral position. It can also be seen that the EKF with the high-level sensor configuration ${}_6\boldsymbol{g}$ provides a better overall accuracy of under 1 % in comparison to the low-level sensor configuration ${}_3\boldsymbol{g}$ with an overall accuracy of under 2 %.

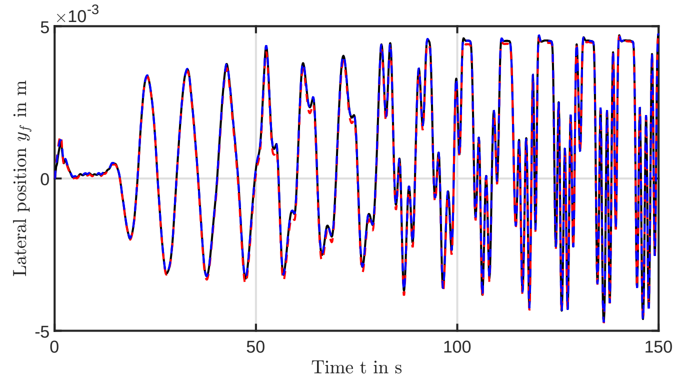

(a) High velocity estimation results based on full order model (15) with low-level ${}_3\boldsymbol{g}$ and high-level sensor configuration ${}_6\boldsymbol{g}$ represented by the dashed red and blue line, respectively.

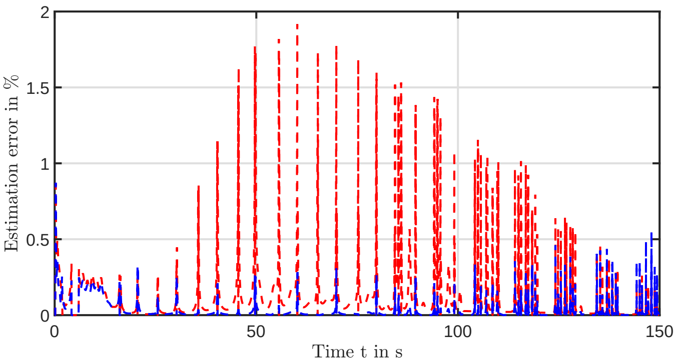

(b) High velocity estimation error based on full order model (15) with low-level ${}_3\boldsymbol{g}$ and high-level sensor configuration ${}_6\boldsymbol{g}$ represented by the dashed red and blue line, respectively.

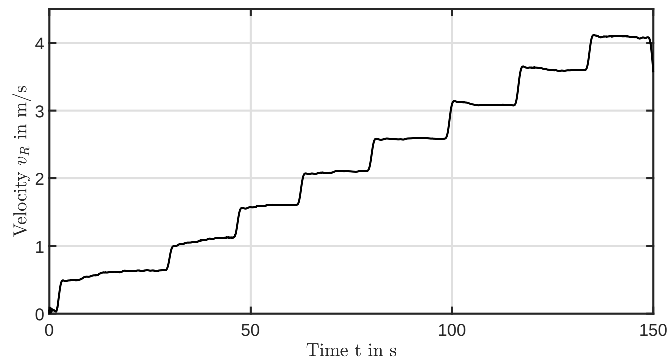

(c) Velocity profile from the measurement shown in Figure 10a.

Figure 10: Results for full order model observer settings with high velocity profile.

In the end, the required accuracy for the estimation of the lateral position during train operation determines the sensor configuration. At this stage of the development non-Gaussian disturbances are not considered. This is probably why the operation of the estimators on the real-time control unit of the running gear on a roller rig needs to be realized with an additional prefiltering of the input signals $\omega_{ms}$ and the FTS. The non-Gaussian disturbances are presumably caused by eccentricities and damages on the running gear wheels. These defects may induce cyclical disturbances in the system. Moreover, these disturbances can be superimposed by similar defects of the rail-profile of the rollers.

## 6. Conclusion

The information of the lateral position of the running gear with IRW is indispensable for the track guidance system in the NGT high speed train concept of the DLR. The direct measurement of the displacement of the wheel-pair is difficult to realize in a practical environment. For this reason, the aim is to design an appropriate observer to estimate this position. To create a reliable estimation system in as many operating states as possible the observability of a full order and a reduced nonlinear system with two different sensor configurations is verified. On this basis EKF observers with U-D formalism are designed. The estimators are synthesized by optimizing the covariance matrices $\boldsymbol{Q}$ and $\boldsymbol{R}$ of the process and measurement noise to get a minimal estimation error for the lateral position. A multi-case optimization with a variation of measured scenarios of the real running gear is used to design the covariance matrices.

The EKFs are implemented in the real-time environment of the running gear testbed and are each validated in operation for two sensor configurations. The obtained experimental results confirm that the observer is well-suited to estimate the lateral position of the running gear. The estimation of the lateral position with the EKF based on the full order system is with an overall accuracy of under 2 % more accurate than the estimation with a reduced model formulation. The estimation accuracy with the high-level sensor configuration is more precise than with the low-level sensor configuration. This means that it depends on the required accuracy of the estimation which sensor configuration has to be chosen.

In the end, it is shown that the observer is able to estimate the lateral position despite wheel flange contact and an unstable behavior of the running gear on the roller rig. In the future we want to implement and test our approach in estimating the lateral position on a full scale running gear with IRW and thus provide the necessary information for the realization of mechatronic track guidance system in the NGT.

## 7. Apendix

The substitutions

$$\begin{aligned}
\vartheta_1 :=& \frac{\xi}{v_R}\left(\dot{y}_f\psi_f + y_f\dot{\psi}_f + y_f\delta_{0,fs}\omega_{fr}\right)\\
&+ \frac{\omega_{fr}r_{fs} - \frac{b}{2}\dot{\psi}_f}{v_R} + 1,\\
\vartheta_2 :=& \frac{\xi}{v_R}\left(\dot{y}_f\psi_f + y_f\dot{\psi}_f - y_f\delta_{0,fs}\omega_{fl}\right)\\
&+ \frac{\omega_{fl}r_{fs} + \frac{b}{2}\dot{\psi}_f}{v_R} + 1,\\
\vartheta_3 :=& \frac{1}{v_R}\left(\dot{\psi}_f + \delta_{0,fs}(\omega_{fr} + \Gamma\dot{y}_f\psi_f)\right),\\
\vartheta_4 :=& \frac{1}{v_R}\left(\dot{\psi}_f - \delta_{0,fs}(\omega_{fl} + \Gamma\dot{y}_f\psi_f)\right),\\
\vartheta_5 :=& \psi_f - \frac{\xi\dot{y}_f\left(1 + \Gamma\delta_{0,fs}y_f\right) + \vartheta_7\dot{\psi}_f}{v_R},\\
\vartheta_6 :=& \psi_f - \frac{\xi\dot{y}_f\left(1 - \Gamma\delta_{0,fs}y_f\right) - \vartheta_8\dot{\psi}_f}{v_R},\\
\vartheta_7 :=& \frac{b\psi_f r_{fs}}{2\left(r_{fs} + r_R + \delta_{0,fs}\xi y_f\right)}, \quad \vartheta_8 = \frac{b\psi_f r_{fs}}{2\left(r_{fs} + r_R - \delta_{0,fs}\xi y_f\right)},
\end{aligned}$$

complete equation (25). The measurement equations (28), (29) und (30) are complemented with the substitutions:

$$\begin{aligned}
\sigma_1 &:= \frac{Gab_{fr}{}^{3/2}c_{23}}{2v_R}\left(\dot{\psi}_f + \delta_{0,fs}(\omega_{fr} + \Gamma\dot{y}_f\psi_f)\right),\\
\sigma_2 &:= \frac{Gab_{fl}{}^{3/2}c_{23}}{2v_R}\left(\dot{\psi}_f - \delta_{0,fs}(\omega_{fl} + \Gamma\dot{y}_f\psi_f)\right),\\
\sigma_3 &:= \frac{g(M_F + M_T)}{4}\left(\frac{2y_f}{b} - 1\right),\\
\sigma_4 &:= \frac{g(M_F + M_T)}{4}\left(\frac{2y_f}{b} + 1\right),\\
\sigma_5 &:= \delta_{0,fs}\left(r_{fs}\Gamma - \xi\delta_{0,fs}{}^2\right)y_f, \quad \sigma_6 = \left(1 + \xi\delta_{0,fs}{}^2\right)y_f,\\
\sigma_7 &:= \frac{Gab_{fr}c_{22}\vartheta_5}{2}, \quad \sigma_8 := \frac{Gab_{fl}c_{22}\vartheta_6}{2},\\
\sigma_9 &:= r_{fs}\left(\delta_{0,fs}{}^2 - 1\right),\\
\sigma_{10} &:= \frac{b\dot{\psi}_f\psi_f r_0}{2v_0(r_{fs} + r_R + \delta_{0,fs}y_f\left(1 + \Gamma\delta_{0,fs}\right))},\\
\sigma_{11} &:= \frac{b\dot{\psi}_f\psi_f r_{fs}}{2v_0(r_{fs} + r_R - \delta_{0,fs}y_f\left(1 + \Gamma\delta_{0,fs}\right))}.
\end{aligned}$$

## References

[1] A. Keck, C. Schwarz, T. Meurer, Observer design for a railway running gear with independently rotating wheels, Vol. 52, 2019, pp. 325 – 330, 8th IFAC Symposium on Mechatronic Systems MECHATRONICS 2019. `doi:https://doi.org/10.1016/j.ifacol.2019.11.695`.

[2] B. Kurzeck, L. Valente, The mechatronic track guiding concept for the DLR "Next Generation Train", in: 8th International Conference on Railway Bogies and Running Gears, 2010, pp. 313–321.

[3] B. Kurzeck, A. Heckmann, C. Wesseler, M. Rapp, Mechatronic track guidance on disturbed track: the trade-off between actuator performance and wheel wear, Vehicle System Dynamics 52 (sup1) (2014) 109–124.

[4] R. Goodall, H. Li, Solid axle and independently-rotating railway wheelsets - a control engineering assessment of stability, Vehicle System Dynamics 33 (1) (2000) 57–67.

[5] T. Mei, H. Li, Control design for the active stabilization of rail wheelsets, Journal of Dynamic Systems, Measurement, and Control 130 (1) (2008) 011002–011002–9.

[6] A. Jaschinski, On the application of similarity laws to a scaled railway bogie model., Ph.D. thesis, TU Delft (1990).

[7] C. Schwarz, A. Heckmann, A. Keck, Different Models of a Scaled Experimental Running Gear for the DLR RailwayDynamics Library, in: 11th International Modelica Conference, 2015, pp. 441–447. `doi:10.3384/ecp15118441`.

[8] A. Heckmann, C. Schwarz, T. Bünte, A. Keck, J. Brembeck, Control development for the scaled experimental railway running gear of DLR, in: 24th IAVSD 2015, Vol. 1 of The Dynamics of Vehicles on Roads and Tracks, CRC Press 2016, 2016, pp. 909–918.

[9] DIN EN 13715:2011-01, Bahnanwendungen - Radsätze und Drehgestelle - Räder - Radprofile [Railway applications - wheelsets and bogies - wheels - wheel profiles] (2011). `doi:10.31030/1727962`.

[10] G. J. Bierman, Measurement updating using the U-D factorization, Automatica 12 (4) (1976) 375–382. `doi:https://doi.org/10.1016/0005-1098(76)90058-3`.

[11] A. Heckmann, A. Keck, I. Kaiser, B. Kurzeck, The Foundation of the DLR RailwayDynamics Library: the Wheel-Rail-Contact, in: 10th International Modelica Conference 2014, Linköping Electronic Conference Proceedings, 2014, pp. 465–475.

[12] J. J. Kalker, Three-Dimensional Elastic Bodies in Rolling Contact, 1st Edition, Kluwer Academic Publishers, Dordrecht, The Netherlands, 1990. `doi:10.1007/978-94-015-7889-9`.

[13] O. Polach, A fast wheel-rail forces calculation computer code, Vehicle System Dynamics 33 (sup1) (1999) 728–739. `doi:10.1080/00423114.1999.12063125`.

[14] K. Knothe, S. Stichel, Rail Vehicle Dynamics, Springer International Publishing, 2017. `doi:10.1007/978-3-319-45376-7`.

[15] J. J. Kalker, A fast algorithm for the simplified theory of rolling contact, Vehicle System Dynamics 11 (1) (1982) 1–13.

[16] K. Popp, W. Schiehlen, Ground Vehicle Dynamics, 1st Edition, Springer-Verlag, Berlin, 2010. `doi:10.1007/978-3-540-68553-1`.

[17] G. Grether, A. Heckmann, G. Looye, Lateral guidance control using information of preceding wheel pairs, in: 26th IAVSD International Symposium on Dynamics of Vehicles on Roads and Tracks, 2019.

[18] R. Hermann, A. Krener, Nonlinear controllability and observability, IEEE Transactions on automatic control 22 (5) (1977) 728–740.

[19] J. P. Gauthier, H. Hammouri, S. Othman, A simple observer for nonlinear systems applications to bioreactors, IEEE Transactions on Automatic Control 37 (6) (1992) 875–880.

[20] D. Simon, Optimal State Estimation: Kalman, H Infinity, and Nonlinear Approaches, Wiley-Interscience, USA, 2006.

[21] G. H. Golub, C. F. Van Loan, Matrix Computations (3rd Ed.), Johns Hopkins University Press, USA, 1996.

[22] G. Bierman, Factorization Methods for Discrete Sequential Estimation, Dover Books on Mathematics Series, Dover Publications, 2006.

[23] H.-D. Joos, J. Bals, G. Looye, K. Schnepper, A. Varga, A multiobjective optimisation-based software environment for control systems design, in: Proceedings of the IEEE International Conference on Control Applications and International Symposium on Computer Aided Control Systems Design, 2002, pp. 7–14.